Open-Set Cross-Domain Hyperspectral Image Classification Based on Manifold Mapping Alignment

Xiangrong Zhang and Baisen Liu

***Abstract*—Cross-scene hyperspectral image (HSI) classification using transfer learning can effectively address the challenge of insufficient labeled samples in classification. The majority of existing transfer learning methods assume consistency in feature labels between the source and target HSI. In practical situations, the target-domain hyperspectral data are likely to contain some categories that do not exist in the source-domain hyperspectral data. In order to solve this problem, this article proposes an unsupervised open-set cross-domain manifold mapping aligned method for target-domain HSI classification. This method designs manifold embedding maps to align the spectral–spatial features of hyperspectral in different scenes. The spectral–spatial feature data are mapped to the subspace using both the source-domain and target-domain mapping matrices. Gradually, target-domain samples are chosen for pseudolabeling within the shared subspace, while samples from unknown classes are rejected. This method achieves subspace learning and pseudolabeled sample updating through iteration, reducing the intraclass distance of all the classes and pushing rejected target data away from known classes. Experiments on the three cross-domain hyperspectral data pairs demonstrate that the proposed method outperforms related state-of-the-art methods.**

***Index Terms*—Domain adaptation, open set, transfer learning.**

I. Introduction

RAPID advancements in computer data processing technology and detector technology have significantly contributed to the development of hyperspectral imaging spectrometers, thereby greatly promoting the field of remote sensing technology [1]. Hyperspectral images (HSIs) captured by hyperspectral remote sensing platforms usually contain dozens or even hundreds of spectral bands [2]. HSIs have the high spectral resolution, and the rich spectral information of HSI can be used for fine-ground object recognition [3]. Due to their rich repository of spectral and spatial information about ground objects, HSIs find broad applications in agriculture [4], [5], military contexts [6], [7], environmental studies [8], ecology [9], and various other fields. HSI feature classification has always been a hot research topic [10], [11], [12]. The evolution from traditional manual features to deep feature extraction [13], [14] has significantly enhanced the performance of remote sensing image feature classification [15]. However, the majority of HSI classification methods focus solely on classifying a single remote sensing image and require sufficient labeled data. In practical situations, the labeling of HSI is time-consuming and laborious. The annotation information in a newly acquired HSI is often limited and cannot directly achieve high-precision classification. Since there are insufficient labeled samples in a single scene, the cross-scene transfer learning method can be used to assist classification with the help of other data with rich labels and similar ground object scenes. Similar labeled samples in the auxiliary data can serve as training samples to classify unlabeled data and transfer sufficient sample information from the source domain to the target scene, thereby achieving the classification of the target scene. However, in practical situations, the acquisition of two sets of data with similar ground objects is often influenced by various factors, including lighting conditions and sensor nonlinearity. Consequently, using sufficient labeled hyperspectral data directly to assist target scene classification may result in negative transfer. Most importantly, there may be classes in the target HSI that are not present in the auxiliary HSI. Therefore, the main purpose of this article is to assist the classification of target scene images by using sufficiently labeled source scene images to improve the classification ability of target scene images while distinguishing unknown categories existing in the target scene images.

The cross-scene HSI classification problem can be regarded as a multimodal problem [16]. The main problem is how to effectively transfer the valuable information of the source field image to the target scene HSI. Since there is spectral drift or spectral mismatch between different HSIs, the main problem is to solve the distribution difference between the auxiliary source hyperspectral data and the target hyperspectral data. With the development of machine learning algorithms, transfer learning can solve the problem of different distributions between the source domain and the target domain [17], [18], [19]. In traditional transfer learning methods, they can be divided into data-centric methods [20] and subspace-centric methods [21], [22]. The joint distribution adaptation method [23] reduced the difference in the marginal and conditional distribution between domains. Cross-domain landmark selection method [24] learns a domain-invariant feature subspace to adapt the distribution of two domains. In the field of remote sensing, Tuia et al. [25]

Manuscript received 8 March 2024; revised 7 April 2024; accepted 15 April 2024. Date of publication 6 May 2024; date of current version 23 May 2024. This work was supported by the Heilongjiang University of Engineering Science and Technology Innovation Team Fund under Grant 2018cx15. *(Corresponding author: Xiangrong Zhang.)*

Xiangrong Zhang is with the School of Management, Heilongjiang Institute of Technology, Harbin 150050, China (e-mail: xiangrongzh@163.com).

Baisen Liu is with the College of Electrical and Information Engineering, Heilongjiang Institute of Technology, Harbin 150050, China.

Digital Object Identifier 10.1109/JSTARS.2024.3396883

proposed a semisupervised manifold alignment method to achieve multimodal remote sensing image classification. Hong et al. [26] improved the classification capabilities of multispectral data by learning the common subspaces of multispectral data and hyperspectral data and using hyperspectral data training. Guo et al. [27] introduced discriminative least squares and learned two different projection matrices to learn the discriminative features between multispectral data and hyperspectral data and achieve collaborative classification of the two. With the rapid development of deep learning, many scholars employ deep networks to align source-domain and target-domain data [28], [29], [30], [31], [32]. A deep adaptation network [32] adopts the multiple-kernel maximum mean discrepancy metric in three adaptive layers to transfer knowledge. Guo et al. [33] utilized the local maximum mean difference to constrain the difference in relevant subdomains between the source domain and the target domain, and achieved good results. Zhang et al. [34] learned nonlocal topological relationships across scene data through a graph convolutional network and aligned the distribution between two scenes through graph optimal transmission. Qu et al. [35] projected the source-domain HSI and target-domain HSI into a shared abundance space through physical features to achieve information migration. However, the above methods all assume that the source-domain hyperspectral data and the target-domain HSI share the same label space.

In actual situations, due to inconsistent shooting scenes, categories that do not exist in the source domain are likely to appear in the target-domain HSI, constituting the open-set problem [36], [37]. In the computer field, Saito et al. [38] realize the identification of unknown classes by designing a backpropagation network. Some scholars [39], [40], [41], [42] realize open-set domain adaptation by improving the transferability between domains. Nevertheless, existing methods are not suitable for remote sensing images because the interclass differences between remote sensing image categories are small. Therefore, this article aims to classify unlabeled target-domain HSIs using labeled source-domain HSIs while also identifying unknown classes and achieving domain adaptation. The main contributions are given as follows. First, a novel manifold embedding alignment algorithm is designed to simultaneously achieve feature alignment of known classes between HSIs and identify unknown class samples. This algorithm maintains the local structural characteristics of samples through manifold structure-preserving constraints in both the source and target domains, significantly reducing the intraclass difference in the subspace. Second, a strategy for identifying unknown class samples is proposed. The algorithm iteratively updates, continuously selects, and rejects pseudolabeled target-domain hyperspectral data. This process aims to enhance classification accuracy, separate unknown classes from known ones, and improve the ability to identify unknown classes.

The rest of this article is organized as follows. Section II provides a detailed introduction to the proposed method. In Section III, we delve into the analysis of the experimental results obtained using the proposed method. In Section IV, the discussion of the proposed method is presented. Finally, Section V concludes this article.

II. Proposed Methods

A. Motivation

Most existing hyperspectral classification methods assume that all training and test data come from the same label space. However, in practical applications, this assumption is often invalid. In such scenarios, traditional classification methods will misclassify unknown categories into known categories. To achieve more accurate classification outcomes, it is essential not only to accurately classify known categories but also to precisely identify unknown categories. Therefore, the primary objective of this article is to effectively leverage the information in the source-domain HSI and transfer it to the target-domain HSI to achieve the accurate separation between known and unknown categories in the target HSI, thereby enhancing classification accuracy.

B. Method Overview

Fig. 1 illustrates the workflow of the proposed method. Initially, the morphological operator is used to extract the multiscale spectral–spatial features of the source-domain hyperspectral data and the target-domain hyperspectral data, where the multiscale spatial spectrum features of the source-domain hyperspectral data are denoted as $\mathbf{X}_s \in \mathbf{R}^{d_s \times n_s}$, and the target-domain hyperspectral spectral–spatial features are denoted as $\mathbf{X}_t \in \mathbf{R}^{d_t \times n_t}$, where n_s and n_t are the number of source and target data samples, respectively, and d_s and d_t are the dimensions of multiscale features. Through the adaptation of multispectral spatial–spectral features of the two domains, the goal of this article is to find two projection matrices $\mathbf{F}_s \in \mathbf{R}^{d_s \times d}$ and $\mathbf{F}_t \in \mathbf{R}^{d_t \times d}$ put the mapped source-domain hyperspectral feature data $\mathbf{Z}_s = \mathbf{F}_s\mathbf{X}_s$ and target-domain hyperspectral feature data $\mathbf{Z}_t = \mathbf{F}_t\mathbf{X}_t$ in the same common subspace. At the same time, pseudolabels are used to iterate, and unknown class data are rejected while continuously optimizing the mapping matrix, thereby achieving feature migration between the source-domain hyperspectral feature data and target-domain hyperspectral data. The method achieves the classification of unknown categories while classifying the known categories of hyperspectral data in the target domain. The main symbols are summarized in Table I for clarity, where matrices are represented by bold entities.

C. Manifold Mapping Alignment

In domain adaptation, it is very important to maintain the structural characteristics of the source domain and the target domain, which can improve the discriminability of extracted features. To maintain the structural information of both the source-domain hyperspectral feature data and the target hyperspectral feature data, constraints are imposed using the manifold information of the spatial–spectral features in the source-domain hyperspectral data and the manifold information of the target-domain hyperspectral features. These constraints ensure that the nearest-neighbor (NN) points of the hyperspectral and target-domain hyperspectral spatial–spectral features in the original space remain close neighbors even after being mapped to the

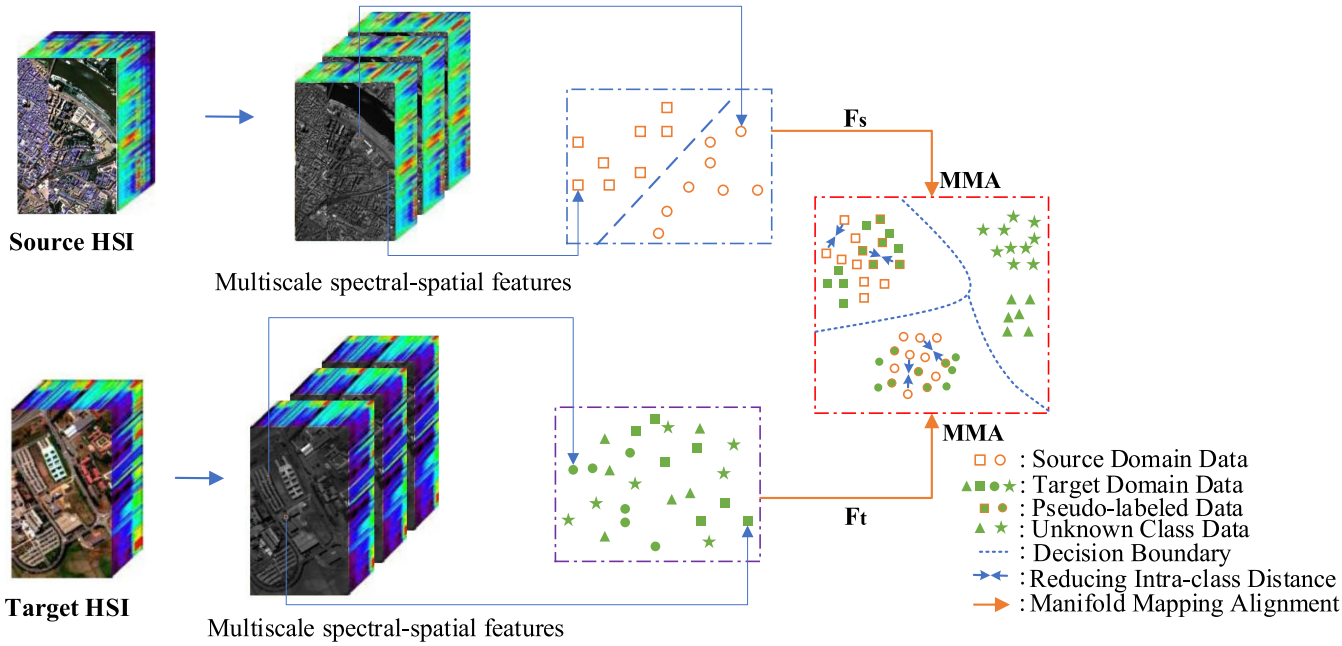

Fig. 1. Workflow of the proposed method.

TABLE I
SUMMARY OF MAIN SYMBOLS

Symbol	Meaning
$\mathbf{x}_i$, $\mathbf{x}_j$	The source/ target samples
$\mathbf{X}_s$, $\mathbf{X}_t$	Source/target samples matrix
$\mathbf{W}_c$ (i,j)	The similarity of the source domain and the target domain
$\mathbf{W}_s$ (i,j)	The similarity of the source domain
$\mathbf{W}_t$ (i,j)	The similarity of the target domain
$\mathbf{Z}_s$, $\mathbf{Z}_t$	Projection matrices of source/target samples
$\mathbf{X}'$	Projected HS and MS samples matrix
$D(z^t, u)$	The Euclidean distance between the two domains
$\mathbf{D}$, $\mathbf{D}_s$, $\mathbf{D}_T$	Diagonal matrices
n_s , n_t	The number of samples in HS/MS images
d_s , d_t	Feature dimensions of source/ target samples
c	Total number of categories
α	Parameter

common subspace. First, the spectral–spatial feature constraints between the source-domain hyperspectral and target-domain hyperspectral cross domains can be expressed as follows:

$$J_c = \sum_{x_i \in S} \sum_{x_j \in T} \left(\mathbf{F}_s^T x_i - \mathbf{F}_t^T x_j\right)^2 \mathbf{W}_c(i,j). \tag{1}$$

In (1), x_i and x_j come from the source-domain hyperspectral data and the target-domain hyperspectral data, respectively. Minimization J_s can align the features between the two domains and $\mathbf{W}_c^{ij}$ measures the similarity between the source domain and the target domain. The similarity matrix is expressed as follows:

$$\mathbf{W}_c(i,j) = \begin{cases} 1 & y_i^s = \hat{y}_j^t \\ 0 & \text{else} \end{cases} \tag{2}$$

where y_i^s represents the label from the source-domain hyperspectral feature, and $\hat{y}_j^t$ represents the pseudolabel of the target-domain spatial spectrum feature. The pseudolabels of target-domain hyperspectral data can be known classes or unknown classes. Before the last iteration of the proposed method, the hyperspectral feature data in the target domain only consider samples that confirm selection or rejection. All other samples are treated as uncertain, with a similarity score of 0 between the uncertain sample and other samples. Similar to the manifold constraints between cross-domain data, source-domain hyperspectral data must maintain the original spatial structure before and after mapping to the subspace. In other words, hyperspectral samples that are far away in the original space will also remain far away after mapping, and vice-versa. Therefore, the manifold constraints of source-domain hyperspectral can be expressed as follows:

$$J_s = \sum_{x_i \in S} \sum_{x_j \in S} \left(\mathbf{F}_s^T x_i - \mathbf{F}_s^T x_j\right)^2 \mathbf{W}_s(i,j) \tag{3}$$

where y_i^s and y_j^s represent the labels from source-domain hyperspectral features. Similarly, the hyperspectral data in the target domain that are closed before mapping must also be closed after mapping. Since the target-domain data do not have labels, pseudolabels are used for constraints. The manifold constraints for target-domain hyperspectral data are given as follows:

$$J_t = \sum_{x_i \in T} \sum_{x_j \in T} \left(\mathbf{F}_t^T x_i - \mathbf{F}_t^T x_j\right)^2 \mathbf{W}_t(i,j). \tag{4}$$

Minimizing the above formula can map points that are originally close in the target-domain closer. The similarity matrix is expressed as follows:

$$\mathbf{W}_t(i,j) = \begin{cases} 1 & \hat{y}_i^t = \hat{y}_j^t \\ 0 & \text{else} \end{cases} \tag{5}$$

where $\hat{y}_i^t$ and $\hat{y}_j^t$ represent the labels from hyperspectral features of the target domain.

D. Pseudolabel Iterative Approach

After calculating the mapping matrix, the source-domain hyperspectral data and the target-domain hyperspectral data can be mapped as follows:

$$\mathbf{Z}_s = \mathbf{F}_s^T \mathbf{X}_s \tag{6}$$

$$\mathbf{Z}_t = \mathbf{F}_t^T \mathbf{X}_t. \tag{7}$$

The data are labeled with pseudolabels by calculating the category average of the multiscale spatial spectrum features. The category average of the features is expressed as follows:

$$u_c = \frac{1}{n_c} \sum_{y_i^s = c} z_i^s \tag{8}$$

where n_c is the number of source-domain hyperspectral data belonging to category C. $D(z^t, u)$ is the Euclidean distance between the target hyperspectral data and the source-domain hyperspectral data; the pseudolabel of the target-domain hyperspectral data can be expressed as follows:

$$\widehat{y}_t = \arg\min_c D(z^t, u). \tag{9}$$

The probability is calculated as follows:

$$p(\widehat{y}_t = c) = \frac{e^{-D(z^t,u)}}{\sum_c e^{-D(z^t,u)}}. \tag{10}$$

Let the total number of runs of the algorithm be T. In the tth cycle, the first $\widehat{y}_t = (t+1)/T$ samples are selected for the next pseudolabel learning. The NN algorithm is used to identify unknown categories. In other words, a hyperspectral sample under test is rejected if its nearest sample in the subspace is a rejected sample. Therefore, through the above algorithm, unknown classes can be distinguished and known classes can be accurately classified.

E. Optimization

Definition $\mathbf{F}^T = [\mathbf{F}_s^T, \mathbf{F}_t^T]$, $\mathbf{X}^T = [\mathbf{X}_s^T, \mathbf{X}_t^T]$, expand J_c, J_s, and J_t

$$\begin{aligned} J_c &= \sum_{\mathbf{x}_i \in S} \sum_{\mathbf{x}_j \in T} \left(\mathbf{F}_s^T \mathbf{x}_i - \mathbf{F}_t^T \mathbf{x}_j\right)^2 \mathbf{W}_c(i,j) \\ &= 2\mathbf{F}^T \mathbf{X}(\mathbf{D} - \mathbf{W})\mathbf{X}^T \mathbf{F} \\ &= 2\mathbf{F}^T \mathbf{X} \mathbf{L} \mathbf{X}^T \mathbf{F} \end{aligned} \tag{11}$$

where $\mathbf{D}$ is a diagonal matrix, $\mathbf{D}(i,j) = \sum_j \mathbf{W}_c(i,j)$, and $\mathbf{L} = \mathbf{D} - \mathbf{W}$ is a Laplacian matrix

$$\begin{aligned} J_s &= \sum_{\mathbf{x}_i \in S} \sum_{\mathbf{x}_j \in S} \left(\mathbf{F}_s^T \mathbf{x}_i - \mathbf{F}_s^T \mathbf{x}_j\right)^2 \mathbf{W}_s(i,j) \\ &= 2\mathbf{F}^T \mathbf{X} \left(\mathbf{D}_S - \mathbf{W}_S\right) \mathbf{X}^T \mathbf{F} \\ &= 2\mathbf{F}^T \mathbf{X} \mathbf{L}_S \mathbf{X}^T \mathbf{F} \end{aligned} \tag{12}$$

where $\mathbf{D}_s$ is the diagonal matrix, $\mathbf{D}_s(i,j) = \sum_j \mathbf{W}_s(i,j)$, $\mathbf{L}_s = \mathbf{D}_s - \mathbf{W}_s$

$$\begin{aligned} J_t &= \sum_{\mathbf{x}_i \in T} \sum_{\mathbf{x}_j \in T} \left(\mathbf{F}_t^T \mathbf{x}_i - \mathbf{F}_t^T \mathbf{x}_j\right)^2 \mathbf{W}_t(i,j) \\ &= 2\mathbf{F}^T \mathbf{X} \left(\mathbf{D}_T - \mathbf{W}_T\right) \mathbf{X}^T \mathbf{F} \\ &= 2\mathbf{F}^T \mathbf{X} \mathbf{L}_T \mathbf{X}^T \mathbf{F} \end{aligned} \tag{13}$$

where $\mathbf{D}_T$ is the diagonal matrix, $\mathbf{D}_T(i,j) = \sum_j \mathbf{W}_t(i,j)$, $\mathbf{L}_T = \mathbf{D}_T - \mathbf{W}_T$.

In summary, the overall objective function can be obtained by adding the above constraints

$$\begin{aligned} &J = J_c + \alpha J_s + (1-\alpha) J_t \\ &= \mathbf{F}^T \mathbf{X} \mathbf{L} \mathbf{X}^T \mathbf{F} + \alpha \mathbf{F}^T \mathbf{X} \mathbf{L}_S \mathbf{X}^T \mathbf{F} + (1-\alpha) \mathbf{F}^T \mathbf{X} \mathbf{L}_T \mathbf{X}^T \mathbf{F} \end{aligned} \tag{14}$$

where the parameter α is used to control the weight contribution of the two constraint items. Therefore, the target vector that needs to be solved in the problem is

$$\begin{aligned} \mathbf{F}^* &= \arg_{\mathbf{F}_s, \mathbf{F}_T} \min J_c + \alpha J_s + (1-\alpha) J_t \\ &= \arg_{\mathbf{F}_s, \mathbf{F}_T} \min \mathbf{F}^T \mathbf{X} \mathbf{L} \mathbf{X}^T \mathbf{F} + \alpha \mathbf{F}^T \mathbf{X} \mathbf{L}_S \mathbf{X}^T \mathbf{F} \\ &\quad + (1-\alpha) \mathbf{F}^T \mathbf{X} \mathbf{L}_T \mathbf{X}^T \mathbf{F}. \end{aligned} \tag{15}$$

It can be seen that the above formula is a generalized Rayleigh quotient problem. According to the mathematical solution method, the solution of this formula is the eigenvector corresponding to the largest generalized eigenvalue

$$\mathbf{X}(\mathbf{L} + \alpha \mathbf{L}_S + (1-\alpha)\mathbf{L}_T)\mathbf{X}^T. \tag{16}$$

When $d > 1$, the transformation projection matrix can be formed by taking the eigenvectors corresponding to the first d largest nonzero eigenvalues.

III. Experimental Results and Result Analysis

A. Data Description

In this section, three sets of hyperspectral datasets, Houston 2013–Houston 2018, PaviaC–PaviaU, and Dioni–Loukia, are employed to verify the effectiveness of the proposed algorithm.

1) Houston 2013–Houston 2018: The first sets of cross-domain datasets are Houston 2018 and Houston 2013 data, in which Houston 2018 data are used as the source domain to classify the target-domain Houston 2013 data. The Houston 2013 data size is 1905 × 349, including a total of 144 spectral bands, and the Houston 2018 data size is 955 × 209, with 48 spectral bands. In order to better conduct experiments, this article selected the 2018 Houston image and the 2013 Houston image of 954 × 209 pixels. Fig. 2 shows the false color map and ground-truth map of the source-domain and target-domain data. The category and quantity settings of the experimental data are shown in Table II.

2) PaviaC–PaviaU: The second dataset is Pavia University (PaviaU) and Pavia Center (PaviaC). In the experiment, PaviaC data are used as source-domain data, and PaviaU data are used as target-domain data. Both the PaviaC and PaviaU sets were acquired by the DAIS hyperspectral sensor. Among them, the

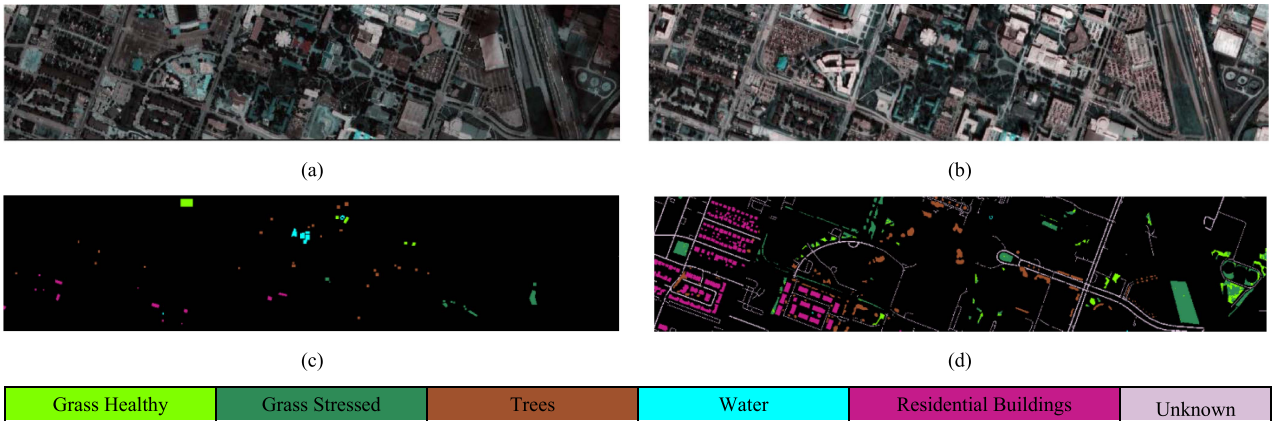

Fig. 2. Pseudocolor image and ground-truth map of Houston 2013–Houston 2018 dataset. (a) Pseudocolor image of Houston 2013. (b) Pseudocolor image of Houston 2018. (c) Ground-truth map of Houston 2013. (d) Ground-truth map of Houston 2018.

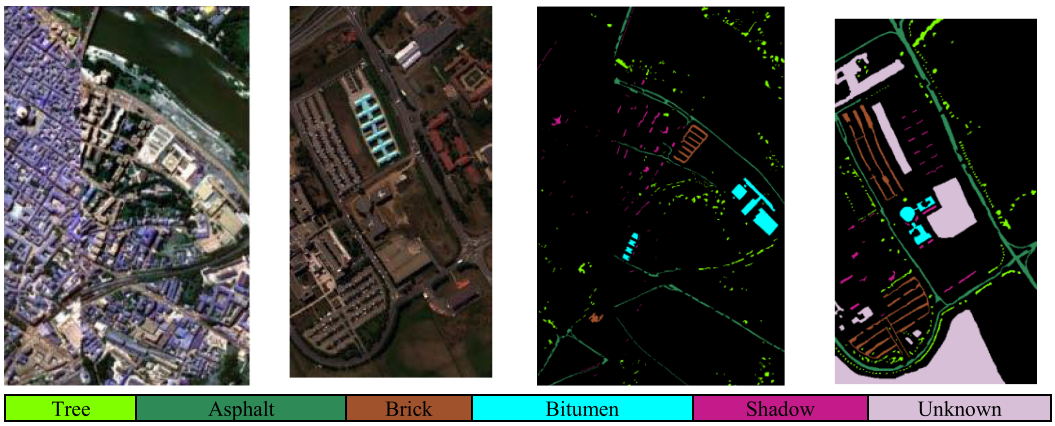

Fig. 3. Pseudocolor image and ground-truth map of PaviaC–PaviaU dataset. (a) Pseudocolor image of PaviaC. (b) Pseudocolor image of PaviaU. (c) Ground-truth map of PaviaC. (d) Ground-truth map of PaviaU.

TABLE II
INFORMATION FOR THE HOUSTON 2013–HOUSTON 2018 DATASET

NO.	Class Name	Training Samples	Test Samples
1	Grass healthy	345	1353
2	Grass stressed	365	4888
3	Trees	365	2766
4	Water	285	22
5	Residential buildings	319	5347
Unk	Unknown	0	6365
Total		1679	20741

TABLE III
INFORMATION FOR THE PAVIAC–PAVIAU DATASET

NO.	Class Name	Training Samples	Test Samples
1	tree	7598	3064
2	Asphalt	9248	6631
3	Brick	2685	3682
4	Bitumen	7282	1330
5	Shadow	2683	947
Unk	Unknown	0	23678
Total		29496	39332

size of the former is 1096 × 715 pixels, and the number of bands is 102. The size of the PaviaU image is 610 × 340 pixels, and the number of spectral bands is 103. The false color maps and ground-truth maps of PaviaU and PaviaC are shown in Fig. 3. Detailed experimental configurations for the datasets are provided in Table III.

3) Dioni–Loukia dataset: The Dioni–Loukia dataset was released by the International Society for Photogrammetry and Remote Sensing (ISPRS) Scientific Initiatives and sourced from the EO-1 satellite, including both Dioni and Loukia datasets. In the experiments of this article, Dioni data serve as source-domain data, and Loukia data are designated as target-domain data. The size of Loukia is 249 × 945 pixels. On the other hand, the Dioni data size is 250 × 1376 pixels. Fig. 4 shows the pseudocolor images in the experiment, while Table IV provides a detailed overview of the experimental data settings.

B. Experimental Setting

The proposed method is compared with four related domain adaptation classification methods, which include close-set domain adaptation methods and open-set domain adaptation methods.

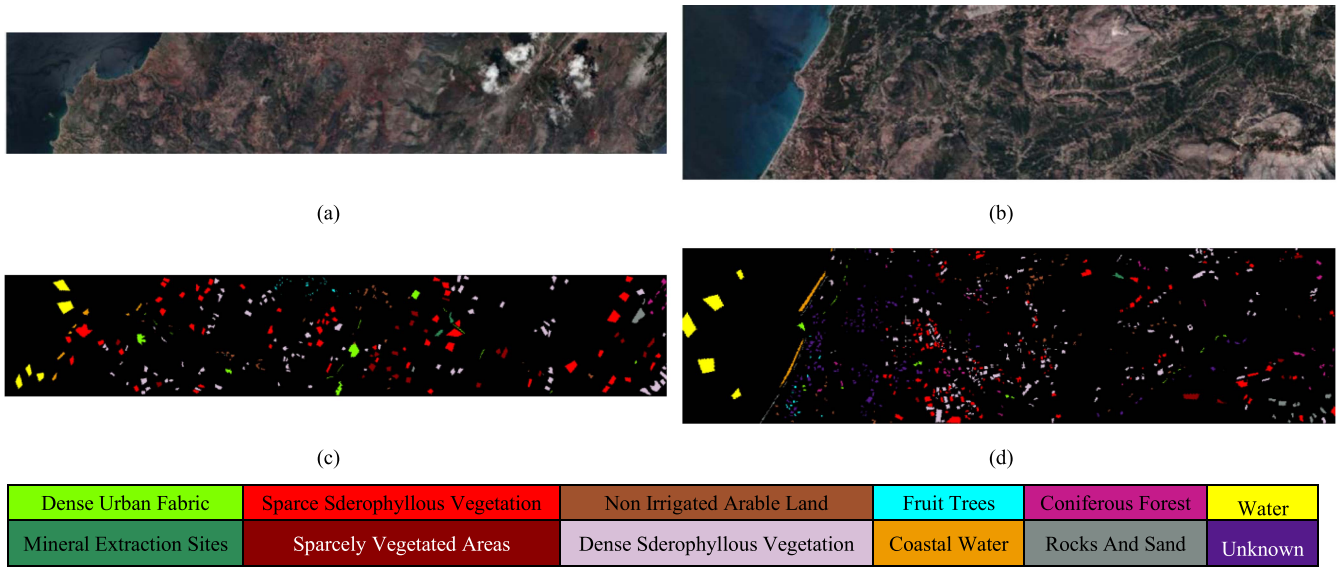

Fig. 4. Pseudocolor image and ground-truth map of Dioni–Loukia dataset. (a) Pseudocolor or image of Dioni. (b) Pseudocolor image of Loukia. (c) Ground-truth map of Dioni. (d) Ground-truth map of Loukia.

TABLE IV
INFORMATION FOR THE DIONI–LOUKIA DATASET

NO.	Class Name	Training Samples	Test Samples
1	Dense Urban Fabric	1262	206
2	Mineral Extraction Sites	204	54
3	Non Irrigated Arable Land	614	426
4	Fruit Trees	150	79
5	Coniferous Forest	361	422
6	Dense Sclerophyll Vegetation	5035	2996
7	Sparse Sclerophyll Vegetation	6374	2361
8	Sparsely Vegetated Areas	1754	399
9	Rocks and Sand	492	453
10	Water	1612	1393
11	Coastal Water	398	421
Unk	Unknown	0	1107
Total		18 256	10 317

1) OSNN [41] is the open-set multiclass classifier that extends upon the NN classifier.
2) JDA+OSNN [23] first uses JDA to align the features of the source domain and the target domain, and then uses OSNN to separate unknown categories.
3) DAOD [39] learns the target classifier to classify unknown classes by optimizing the structural risk function, joint distribution, and open-set difference.
4) OSDA-ETD [42] identifies unknown classes by reducing local and global distribution differences. In order to ensure the fairness of the experiment, we use the optimal parameters. In the method proposed in this article, we set the subspace dimension to 30.

C. Evaluation Index

We use overall accuracy (OA) and Kappa coefficient (KC) to evaluate the classification effect, respectively. For the evaluation of open-set classification, we adopt the same evaluation as previous work, namely class-specific accuracy (CA), OS, OS$*$, and HOS. HOS is the harmonic mean of OS$*$ and Unk. Unk is the classification accuracy of the unknown class. The specific expressions of the evaluation indicators are given as follows:

$$\mathrm{CA} = \frac{\left|\mathbf{x} : \mathbf{x} \in \mathcal{D}_t^i \wedge \widehat{y}(\mathbf{x}) = i\right|}{\left|\mathbf{x} : \mathbf{x} \in \mathcal{D}_t^i\right|} \tag{17}$$

$$\mathrm{UNK} = \frac{\left|x : x \in \mathcal{D}_t^{\mathrm{unk}} \wedge \hat{y}(x) = \mathrm{unk}\right|}{\left|x : x \in \mathcal{D}_t^{\mathrm{unk}}\right|} \tag{18}$$

$$\mathrm{OS}^* = \frac{1}{C}\sum_{i=1}^{C} \frac{\left|\mathbf{x} : \mathbf{x} \in \mathcal{D}_t^i \wedge \hat{y}(x) = i\right|}{\left|\mathbf{x} : \mathbf{x} \in \mathcal{D}_t^i\right|} \tag{19}$$

$$\mathrm{OS} = \frac{1}{C+1}\sum_{i=1}^{C+1} \frac{\left|\mathbf{x} : \mathbf{x} \in \mathcal{D}_t^i \wedge \hat{y}(x) = i\right|}{\left|\mathbf{x} : \mathbf{x} \in \mathcal{D}_t^i\right|} \tag{20}$$

$$\mathrm{HOS} = \frac{2 \times \mathrm{OS}^* \times \mathrm{UNK}}{\mathrm{OS}^* + \mathrm{UNK}}. \tag{21}$$

D. Compared With Other Methods

This section uses three cross-domain HSI datasets, the Houston 2013–Houston 2018 dataset, the Dioni–Loukia dataset, and the PaviaC–PaviaU dataset, to verify the effectiveness of the proposed method. To prevent unexpected errors, we conducted ten independent experiments and calculated the average accuracy. In each set of experiments, 5% of the samples from the source-domain hyperspectral data were employed for classifying the target hyperspectral data. The experimental results are shown in Tables V–VII, with the best classification result in each row highlighted in bold. As shown in Table V, showing the classification results of the Houston 2013–Houston 2018 dataset, it can be seen that the proposed method has a closed-set

TABLE V
CLASSIFICATION RESULTS ON THE HOUSTON 2013–HOUSTON 2018 DATASET

Class	OSNN	JDA	DAOD	OSDA-ETD	Ours
1	51.44	60.79	84.92	68.14	**74.50**
2	60.63	**62.64**	38.60	47.23	57.59
3	53.43	62.11	44.75	51.84	**63.05**
4	100	100	100	100	100
5	65.32	70.68	**82.42**	74.62	78.90
Unknown	33.52	14.39	36.54	57.94	**59.84**
OS	60.73	61.77	64.5	68.30	**72.31**
OS*	66.17	71.25	70.1	66.63	**74.81**
HOS	44.5	23.95	48.05	61.83	**66.49**
OA	52.01	49.60	53.20	62.68	**65.65**
Kappa	0.3986	0.3823	0.42	0.5105	**0.5574**

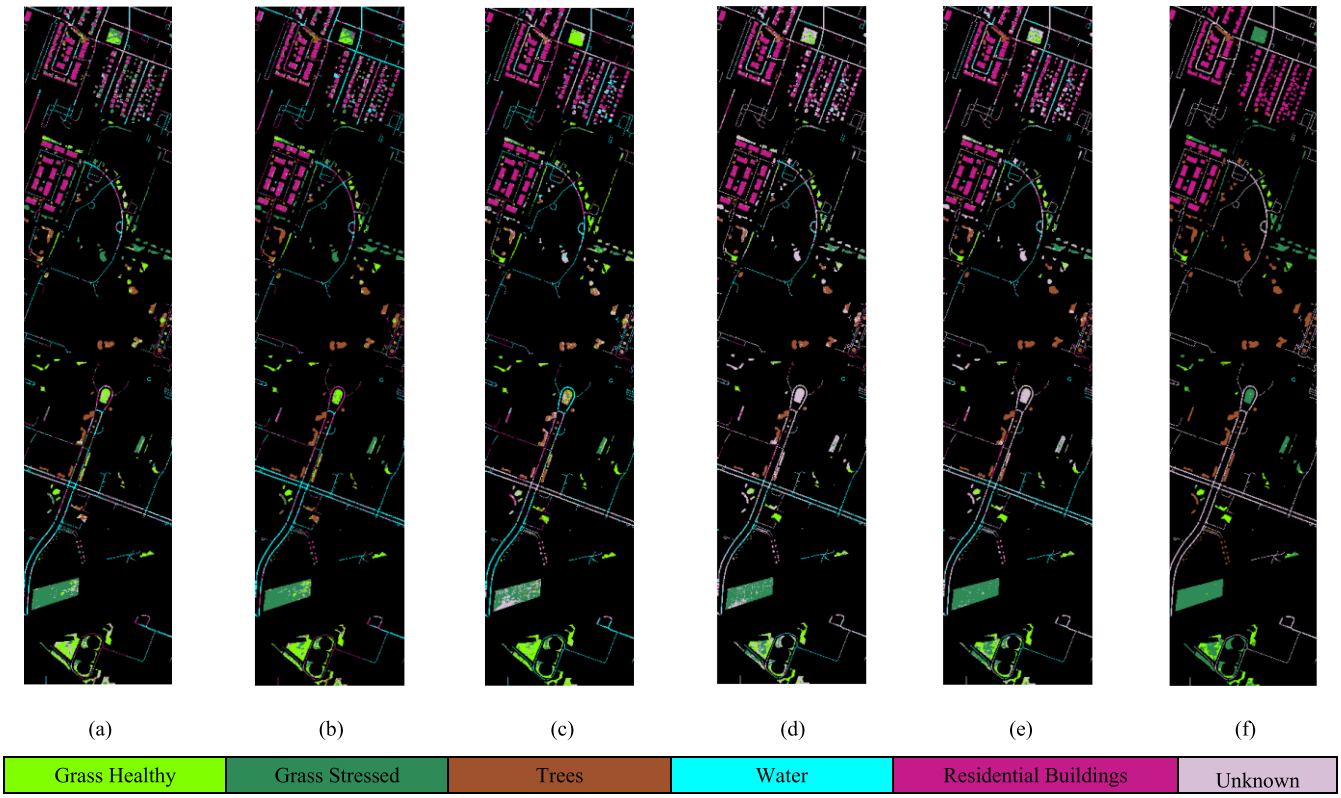

Fig. 5. Classification map on the Houston 2013–Houston 2018 dataset. (a) OSNN. (b) JDA. (c) DAOD. (d) OSDA-ETD. (e) Ours. (f) Ground-truth map.

evaluation index OS$*$ higher than the second highest method OSDA-ETD about 8.18%.

In the open-set evaluation indicators, HOS and OS are 4.01% and 4.66% higher than OSDA-ETD, respectively. It can be seen that the HOS index of the JDA method is the lowest at only 23.95%. The JDA method has the worst classification effect on the location category, with an accuracy of only 14.39%. This is because the JDA method is designed for transfer learning of closed sets. When unknown classes appear, the JDA method cannot better adapt the source domain and the target domain, and thus cannot achieve good classification results. DAOD, OSDA-ETD, and the proposed classification method all perform better than OSNN, which shows that the distribution and data alignment between domains are very important in cross-domain open-set classification. In order to further demonstrate the classification effect of the proposed method, the classification maps are shown in Fig. 5. It can be seen that the proposed method is closest to the true value map. In the blue rectangular box, most methods divide unknown classes into residential buildings' classes. In the red rectangular box, the OSNN method, JDA method, and DAOD method misclassify the trees category into the grass healthy category, which may be due to some similarity in the spectra between them. It can be seen that the proposed method is significantly better than the other domain adaptive methods. Tables VI and Fig. 6 show the classification results and classification maps of the PaviaC–PaviaU dataset. It can be seen that the proposed method achieves the optimal effect in all evaluation indicators, and the classification accuracy of the method is the highest for most categories. The OS of the proposed method reaches 83.73%, which is better than the second-highest method

TABLE VI
CLASSIFICATION RESULTS ON THE PAVIAC–PAVIAU DATASET

Class	OSNN	JDA	DAOD	OSDA-ETD	Ours
1	99.28	99.57	99.60	99.47	**99.60**
2	79.33	81.66	80.86	75.47	**84.18**
3	86.47	90.44	84.67	**92.20**	90.52
4	65.11	57.06	61.72	63.83	**73.45**
5	99.68	99.68	**99.89**	99.68	**99.89**
Unknown	22.72	16.39	43.20	38.71	**54.70**
OS	75.44	74.14	78.33	78.23	**83.73**
OS*	85.98	85.69	85.35	86.14	**89.53**
HOS	35.94	27.53	57.37	53.42	**67.91**
OA	47.4855	44.193	59.82	56.97	**68.24**
Kappa	0.3563	0.3162	0.4592	0.4373	**0.5583**

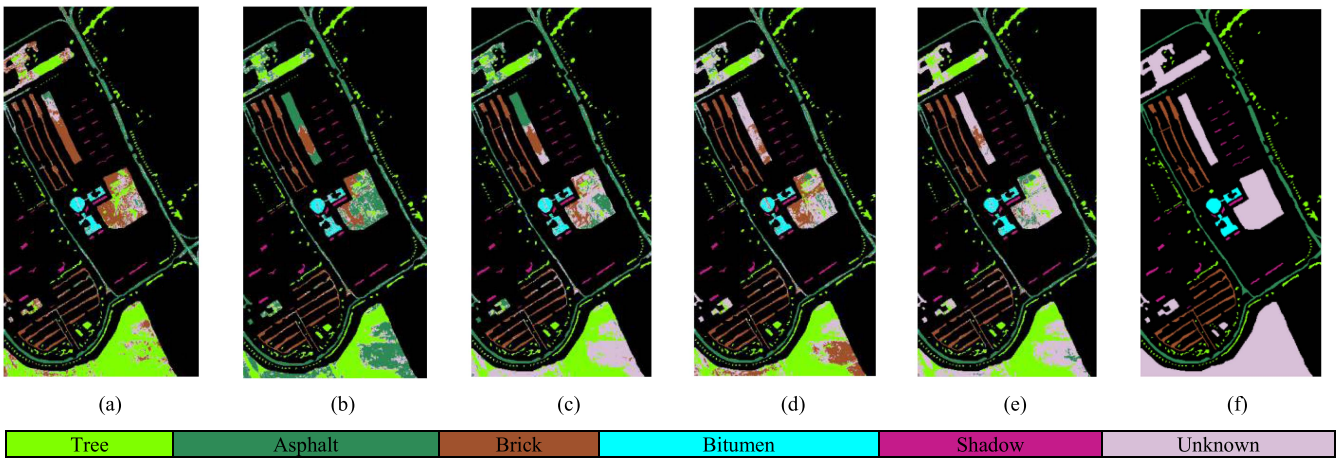

Fig. 6. Classification map on the PaviaC–PaviaU dataset. (a) OSNN. (b) JDA. (c) DAOD. (d) OSDA-ETD. (e) Ours. (f) Ground-truth map.

TABLE VII
CLASSIFICATION RESULTS ON THE DIONI–LOUKIA DATASET

Class	OSNN	JDA	DAOD	OSDA-ETD	Ours
1	16.50	3.39	11.16	13.60	**16.51**
2	44.44	88.88	7.40	68.50	**68.51**
3	45.77	38.96	38.26	46.24	**49.29**
4	2.53	25.31	6.32	**27.84**	20.25
5	31.75	40.28	46.44	38.38	**54.02**
6	67.72	**78.17**	67.82	77.43	72.53
7	67.04	23.33	67.30	66.7	**72.55**
8	19.04	36.84	44.86	**47.86**	43.35
9	56.73	9.4923	78.58	70.19	**96.02**
10	**100**	**100**	**100**	**100**	**100**
11	**100**	**100**	**100**	**100**	**100**
Unknown	26.91	11.47	43.17	40.65	**50.76**
OS	48.21	46.35	50.95	58.12	**61.99**
OS*	50.14	49.52	51.65	59.71	**63.01**
HOS	35.03	18.63	47.04	47.04	**56.23**
OA	62.47	52.68	66.28	68.95	**71.67**
Kappa	0.5417	0.4337	0.5908	0.4837	**0.6573**

OSDA-ETD. The OS$*$ accuracy of the OSDA-ETD method is better than that of DAOD. Among all classification methods, the JDA method achieved the worst results, which may be due to the phenomenon of negative transfer caused by the emergence of unknown categories. The classification accuracy of the proposed method for unknown categories reaches 54.7%, which is better than the comparable cross-domain open-set classification method. It shows that the proposed method can adapt the source domain and the target domain and effectively separate unknown samples, thereby achieving better classification results. In the classification maps, it can also be seen that our method, the classification map, of the method proposed in this article has less noise and is smoother. For the Dioni–Loukia dataset, the classification results are shown in Table VII and Fig. 7. It can be seen that among these three sets of cross-scenario HSI datasets, the classification results of Loukia are relatively poor. This may be because the spectra of some ground objects in this dataset are relatively similar, and the degree of distinction is significantly

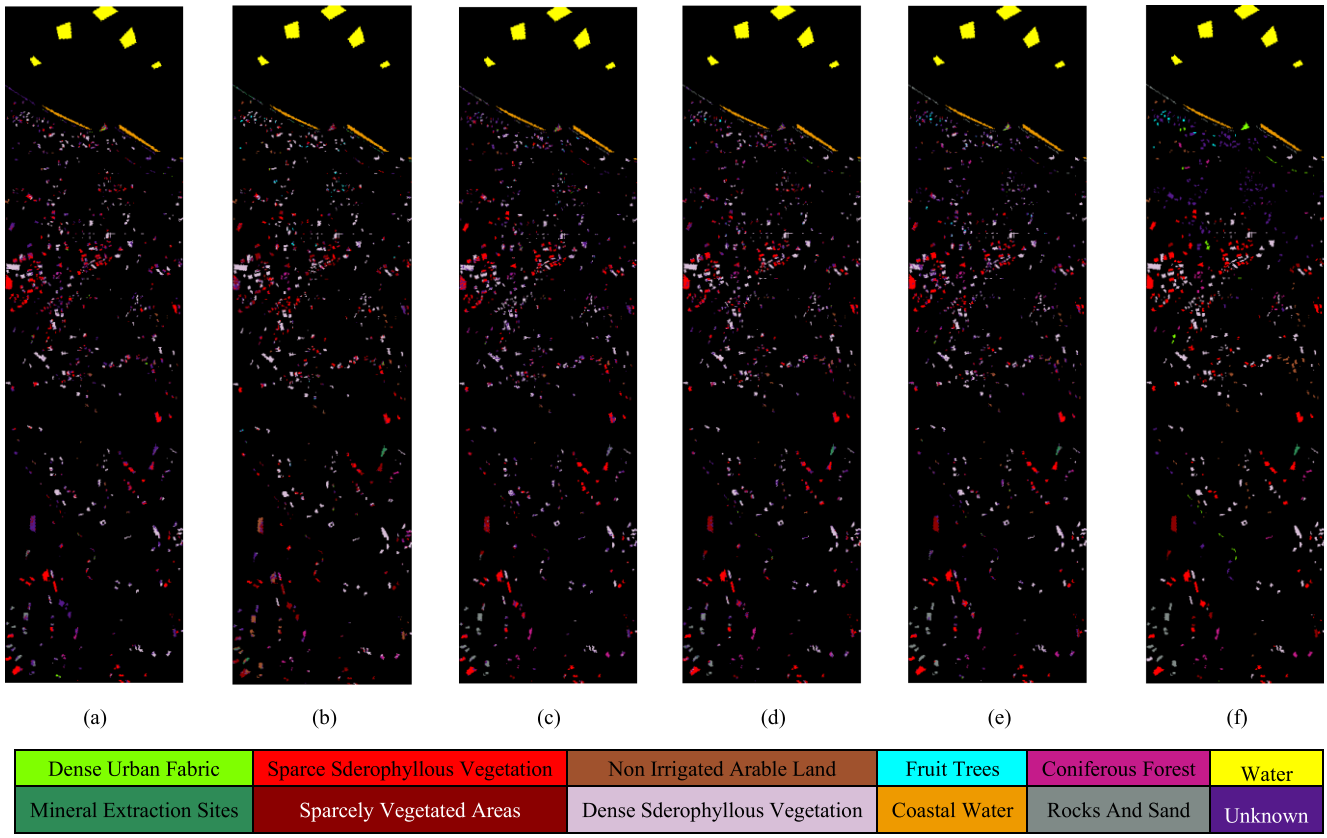

Fig. 7. Classification map on the Dioni–Loukia dataset. (a) OSNN. (b) JDA. (c) DAOD. (d) OSDA-ETD. (e) Ours. (f) Ground-truth map.

lower than that of urban scene data, such as the fourth type of Fruit Trees and the fifth type of Coniferous Forest. However, it can be seen that the method proposed in this article still achieves the optimal classification results. The proposed method achieves the best results on all evaluation indicators of OS, OS$*$, HOS, OA, and Kappa. Similar to the Houston dataset results, the JDA method has the worst classification effect on unknown categories, followed by the OSNN method. Although the classification accuracy of the JDA method for unknown categories is lower than OSNN, other categories are better than OSNN, which shows that the probabilistic adaptation between the source domain and the target domain is very important. Our method demonstrates the best classification effectiveness for unknown categories at 50.76% while achieving an overall accuracy of 71.6%. Our method closely approximates the ground-truth map. In the OSDA-ETD method, most of the unknown classes in the lower half of the image are mistakenly divided into tree and brick classes, while the JDA method hardly separates all unknown classes. The OSDA-ETD method is better than the DAOD method, indicating that the OSDA-ETD method effectively reduces local and global distribution differences between the source domain and the target domain. In the classification result maps, as shown in Fig. 7, most of the Rocks and Sand categories are mistakenly classified into the nonirrigated arable land category in the JDA method, and some of the sparsely vegetated areas' categories are mistakenly classified into the unknown category in the OSNN method. It can be seen from Fig. 7 that the classification results of the method proposed in this article are closest to the true value map, especially in the rectangular frame part, which proves the superiority of the proposed method.

IV. Discussion

A. Alignment Performance

In order to further demonstrate the proposed method, the t-SNE maps are used to map the features before classification. As shown in Figs. 8–10, the source-domain data are represented by "·", and the target-domain data are represented by "+." As can be seen in Fig. 8, our method adapts the source domain and the target domain. The intraclass distance between different categories is reduced and the interclass distance is increased. As shown in the figure, our method gathers unknown categories together after mapping, which can better distinguish them from other categories and reduce aliasing. It can be seen that, in the OSNN method and the JDA method, the unknown category and the Grass Healthy category are seriously aliased, so the unknown class is mistakenly divided into the class Grass Healthy and class Trees in the classification map. In the OSDA-ETD method, some unknown categories and class Trees are mixed, which also lead to the misclassification of the two categories. It can be seen in Fig. 9 that our method perfectly adapts the source-domain and target-domain data of the same category, such as the class Grass

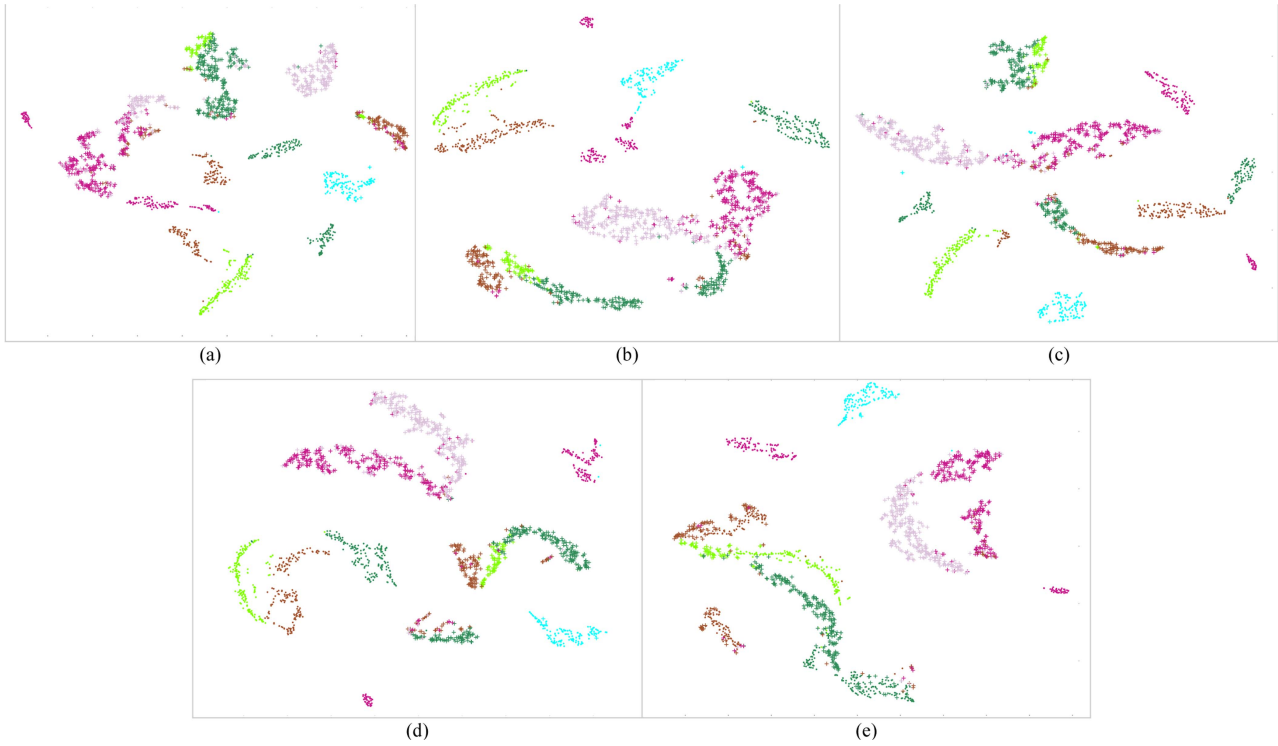

Fig. 8. t-SNE maps of the Houston 2013–Houston 2018 dataset. (a) OSNN. (b) JDA. (c) DAOD. (d) OSDA-ETD. (e) Ours.

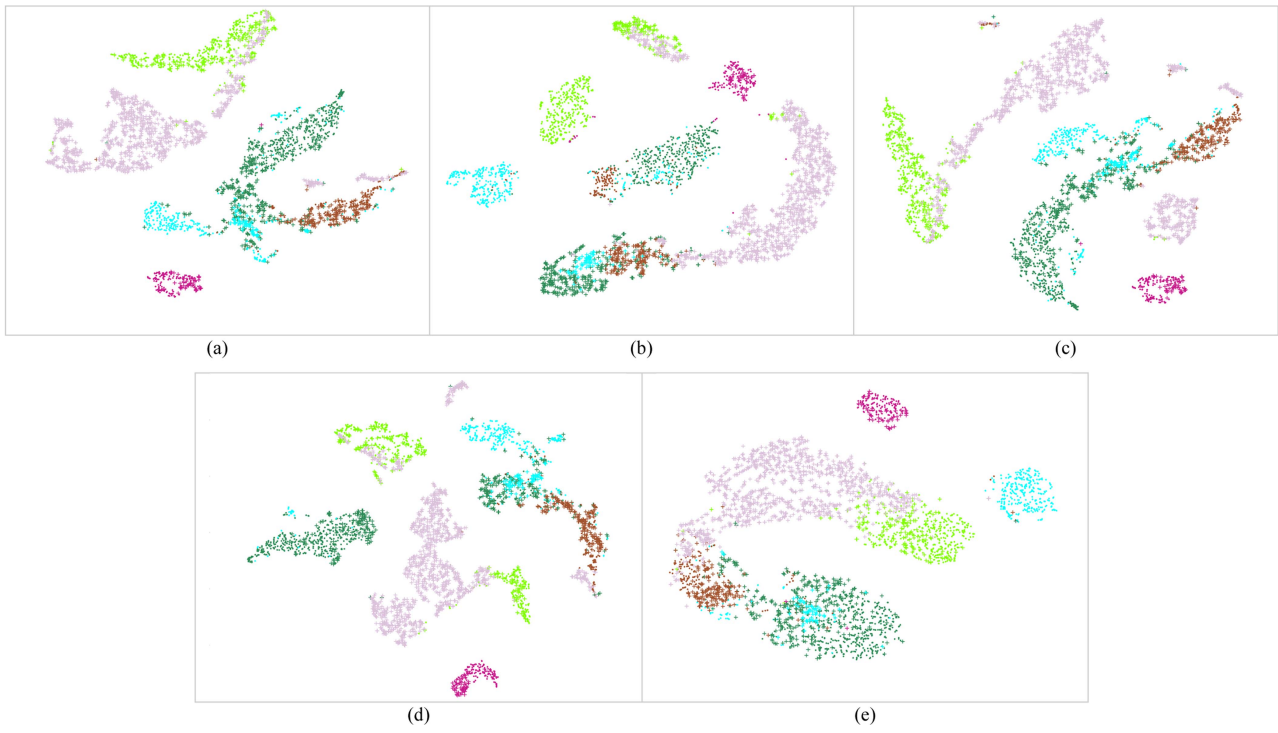

Fig. 9. t-SNE maps of the Houston 2013–Houston 2018 dataset. (a) OSNN. (b) JDA. (c) DAOD. (d) OSDA-ETD. (e) Ours.

healthy and Grass stressed and Trees, effectively reducing the intraclass distance. For unknown categories, the method proposed in this article further distinguishes unknown categories from other known categories and also clusters unknown categories together. Therefore, the method proposed in this article achieves better classification results. Fig. 10 displays the mapping results obtained from the Houston datasets. In the map, aliasing is observed among most categories, with particularly severe aliasing in the JDA method. This highlights that, when unknown categories are present, domain adaptation methods designed for

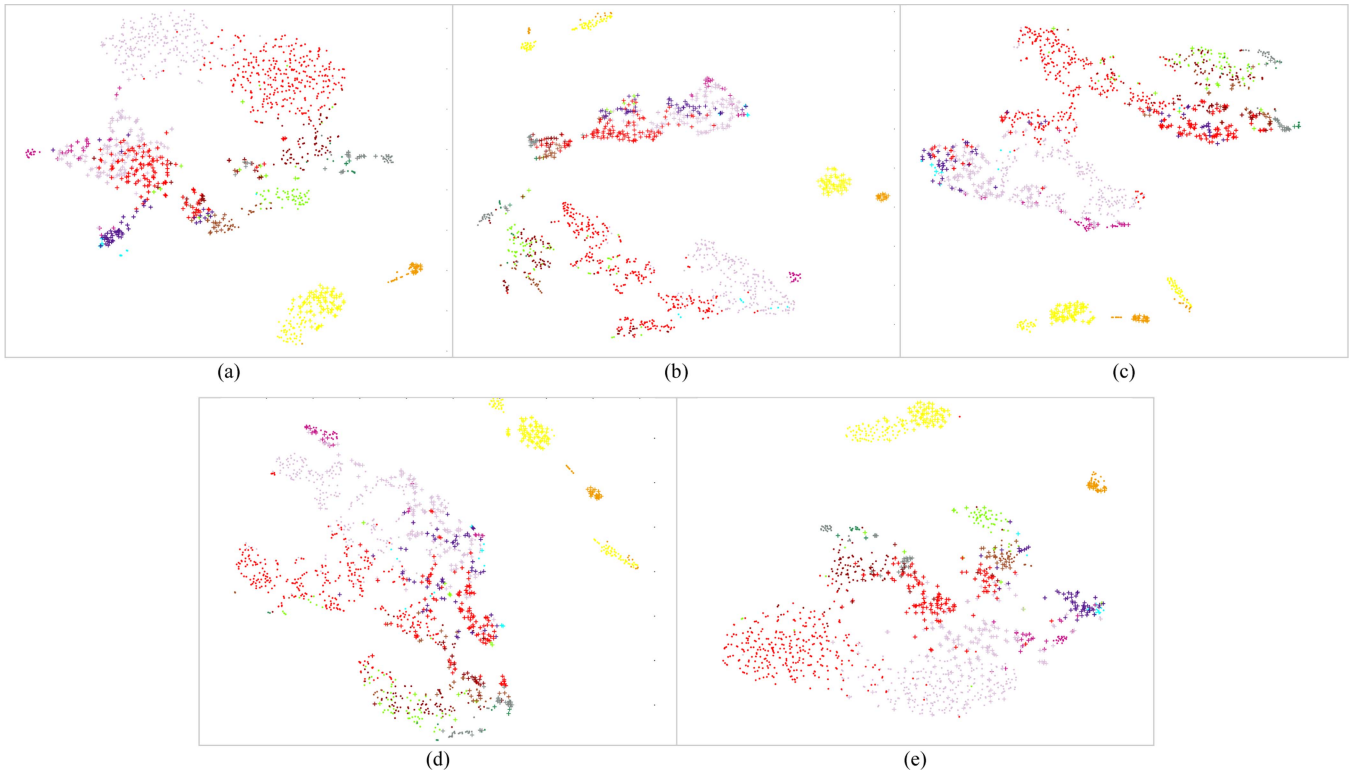

Fig. 10. t-SNE maps of the Houston 2013–Houston 2018 dataset. (a) OSNN. (b) JDA. (c) DAOD. (d) OSDA-ETD. (e) Ours.

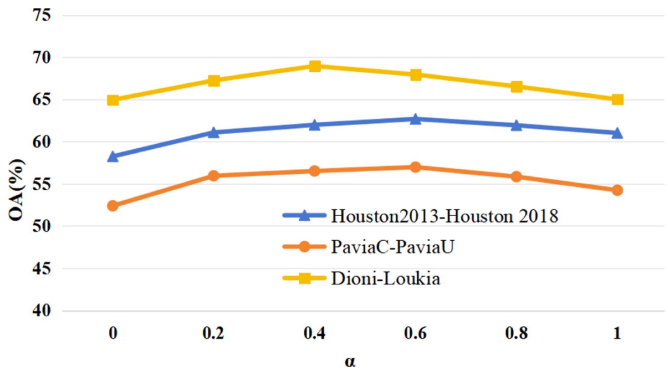

Fig. 11. Parameter sensitivity analysis on three datasets.

closed sets may struggle to effectively adapt between the source domain and the target domain. The method proposed in this article distinguishes most categories and reduces the distance between the source domain and the target domain, such as the class Dense Sclerophyllous Vegetation and the class Sparce Sclerophyllous Vegetation.

B. Parameter Sensitivity

The proposed method mainly involves the parameter α used to control the weight contribution of the two constraint items from the source domain and the target domain. As shown in Fig. 11, it demonstrates the impact of changing the parameters within the appropriate range on the OAs' indicators of the three datasets. Specifically, the optimal parameter α for the Houston 2013–Houston 2018 dataset is 0.4, while it is 0.6 for both the PaviaC–PaviaU and Dioni–Loukia datasets. In the experiment, we used these optimal parameters.

V. Conclusion

In this article, we propose a cross-domain open-set classification method, which breaks the bottleneck of existing transfer learning methods that can only perform closed-set classification. The method proposed in this article first extracts multiscale spatial–spectral features of the source-domain hyperspectral data and target-domain hyperspectral data, and then proposes manifold embedding mapping alignment to adapt the features between source-domain hyperspectral and target-domain HSIs. By learning two mapping matrices, the feature data of the two domains are mapped into a common subspace. At the same time, the proposed method assigns pseudolabels to the target hyperspectral data through step-by-step iteration and selection. Through gradual iteration, the feature data of the source domain and the target domain are continuously adapted, pushing the unknown category data away from the known category data, reducing the intracategory distance, and improving the discriminability of the features. Compared with the state-of-the-art methods, the method proposed in this article achieves better results on three sets of hyperspectral datasets, indicating the effectiveness of the method proposed in this article. In the future, we will conduct research on open-set classification of cross-modal data.

REFERENCES

[1] P. Ghamisi et al., "Advances in hyperspectral image and signal processing: A comprehensive overview of the state of the art," *IEEE Geosci. Remote Sens. Mag.*, vol. 5, no. 4, pp. 37–78, Dec. 2017.

[2] P. Ghamisi et al., "New frontiers in spectral–spatial hyperspectral image classification: The latest advances based on mathematical morphology Markov random fields segmentation sparse representation and deep learning," *IEEE Geosci. Remote Sens. Mag.*, vol. 6, no. 3, pp. 10–43, Sep. 2018.

[3] M. Fauvel, Y. Tarabalka, J. A. Benediktsson, J. Chanussot, and J. C. Tilton, "Advances in spectral-spatial classification of hyperspectral images," *Proc. IEEE*, vol. 101, no. 3, pp. 652–675, Mar. 2013.

[4] C. M. Gevaert, J. Suomalainen, J. Tang, and L. Kooistra, "Generation of spectral–temporal response surfaces by combining multispectral satellite and hyperspectral UAV imagery for precision agriculture applications," *IEEE J. Sel. Topics Appl. Earth Observ. Remote Sens.*, vol. 8, no. 6, pp. 3140–3146, Jun. 2015.

[5] L. Yang, R. Zhang, Y. Bao, S. Yang, and L. Jiao, "Kernel tensor sparse coding model for precise crop classification of UAV hyperspectral image," *IEEE Geosci. Remote Sens. Lett.*, vol. 20, Oct. 2023, Art. no. 5511405, doi: 10.1109/LGRS.2023.3326452.

[6] M. Shimoni, R. Haelterman, and C. Perneel, "Hyperspectral imaging for military and security applications: Combining myriad processing and sensing techniques," *IEEE Geosci. Remote Sens. Mag.*, vol. 7, no. 2, pp. 101–117, Jun. 2019.

[7] I. Makki, R. Younes, C. Francis, T. Bianchi, and M. Zucchetti, "A survey of landmine detection using hyperspectral imaging," *ISPRS J. Photogramm. Remote Sens.*, vol. 124, pp. 40–53, Feb. 2017.

[8] C.-I. Chang, *Hyperspectral Data Exploitation: Theory and Applications*. New York, NY, USA: Wiley, 2007.

[9] J. M. Bioucas-Dias, A. Plaza, G. Camps-Valls, P. Scheunders, N. Nasrabadi, and J. Chanussot, "Hyperspectral remote sensing data analysis and future challenges," *IEEE Geosci. Remote Sens. Mag.*, vol. 1, no. 2, pp. 6–36, Jun. 2013.

[10] Y. Gu, T. Liu, and J. Li, "Superpixel tensor model for spatial–spectral classification of remote sensing images," *IEEE Trans. Geosci. Remote Sens.*, vol. 57, no. 7, pp. 4705–4719, Jul. 2019, doi: 10.1109/TGRS.2019.2892516.

[11] B. Guo, T. Liu, and Y. Gu, "Integrating coupled dictionary learning and distance preserved probability distribution adaptation for multispectral–hyperspectral image collaborative classification," *IEEE Trans. Geosci. Remote Sens.*, vol. 60, Apr. 2022, Art. no. 5528013.

[12] T. Liu, Y. Gu, and X. Jia, "Class-guided coupled dictionary learning for multispectral-hyperspectral remote sensing image collaborative classification," *Sci. China Technol. Sci.*, vol. 65, pp. 744–758, 2022.

[13] J. Xia, M. Dalla Mura, J. Chanussot, P. Du, and X. He, "Random subspace ensembles for hyperspectral image classification with extended morphological attribute profiles," *IEEE Trans. Geosci. Remote Sens.*, vol. 53, no. 9, pp. 4768–4786, Sep. 2015, doi: 10.1109/TGRS.2015.2409195.

[14] L. Fang, N. He, S. Li, P. Ghamisi, and J. A. Benediktsson, "Extinction profiles fusion for hyperspectral images classification," *IEEE Trans. Geosci. Remote Sens.*, vol. 56, no. 3, pp. 1803–1815, Mar. 2018, doi: 10.1109/TGRS.2017.2768479.

[15] Q. Yuan et al., "Deep learning in environmental remote sensing: Achievements and challenges," *Remote Sens. Environ.*, vol. 241, 2020, Art. no. 111716.

[16] Y. Gu et al., "Multimodal hyperspectral remote sensing: An overview and perspective," *Sci. China Inf. Sci.*, vol. 64, Feb. 2021, Art. no. 121301.

[17] S. J. Pan, I. W. Tsang, J. T. Kwok, and Q. Yang, "Domain adaptation via transfer component analysis," *IEEE Trans. Neural Netw.*, vol. 22, no. 2, pp. 199–210, Feb. 2011, doi: 10.1109/TNN.2010.2091281.

[18] H. Wang, F. Nie, H. Huang, and C. Ding, "Dyadic transfer learning for cross-domain image classification," in *Proc. Int. Conf. Comput. Vis.*, 2011, pp. 551–556.

[19] L. Cheng and S. J. Pan, "Semi-supervised domain adaptation on manifolds," *IEEE Trans. Neural Netw. Learn. Syst.*, vol. 25, no. 12, pp. 2240–2249, Dec. 2014, doi: 10.1109/TNNLS.2014.2308325.

[20] M. G. Rahman and M. Z. Islam, "A framework for supervised heterogeneous transfer learning using dynamic distribution adaptation and manifold regularization," *IEEE Trans. Serv. Comput.*, vol. 16, no. 3, pp. 1555–1571, May/Jun. 2023, doi: 10.1109/TSC.2022.3213238.

[21] Q. Tian, H. Sun, C. Ma, M. Cao, Y. Chu, and S. Chen, "Heterogeneous domain adaptation with structure and classification space alignment," *IEEE Trans. Cybern.*, vol. 52, no. 10, pp. 10328–10338, Oct. 2022.

[22] S. J. Pan and Q. Yang, "A survey on transfer learning," *IEEE Trans. Knowl. Data Eng.*, vol. 22, no. 10, pp. 1345–1359, Oct. 2010.

[23] M. Long, J. Wang, G. Ding, J. Sun, and P. S. Yu, "Transfer feature learning with joint distribution adaptation," in *Proc. IEEE Int. Conf. Comput. Vis.*, 2013, pp. 2200–2207.

[24] Y. H. Tsai, Y. Yeh, and Y. F. Wang, "Learning cross-domain landmarks for heterogeneous domain adaptation," in *Proc. IEEE Conf. Comput. Vis. Pattern Recognit.*, 2016, pp. 5081–5090.

[25] D. Tuia, M. Volpi, M. Trolliet, and G. Camps-Valls, "Semisupervised manifold alignment of multimodal remote sensing images," *IEEE Trans. Geosci. Remote Sens.*, vol. 52, no. 12, pp. 7708–7720, Dec. 2014.

[26] D. Hong, J. Chanussot, N. Yokoya, J. Kang, and X. X. Zhu, "Learning-shared cross-modality representation using multispectral-LiDAR and hyperspectral data," *IEEE Geosci. Remote. Sens. Lett.*, vol. 17, no. 8, pp. 1470–1474, Aug. 2020.

[27] B. Guo, T. Liu, and Y. Gu, "Structure preserved discriminative distribution adaptation for multihyperspectral image collaborative classification," *IEEE Trans. Geosci. Remote Sens.*, vol. 61, Sep. 2023, Art. no. 5526815, doi: 10.1109/TGRS.2023.3315472.

[28] D. Hong et al., "More diverse means better: Multimodal deep learning meets remote-sensing imagery classification," *IEEE Trans. Geosci. Remote Sens.*, vol. 59, no. 5, pp. 4340–4354, May 2021.

[29] D. Hong, J. Yao, D. Meng, Z. Xu, and J. Chanussot, "Multimodal GANs: Toward crossmodal hyperspectral–multispectral image segmentation," *IEEE Trans. Geosci. Remote Sens.*, vol. 59, no. 6, pp. 5103–5113, Jun. 2021.

[30] J. Yang, Y.-Q. Zhao, and J. C.-W. Chan, "Learning and transferring deep joint spectral–spatial features for hyperspectral classification," *IEEE Trans. Geosci. Remote Sens.*, vol. 55, no. 8, pp. 4729–4742, Aug. 2017.

[31] B. Liu, X. Yu, A. Yu, P. Zhang, G. Wan, and R. Wang, "Deep few-shot learning for hyperspectral image classification," *IEEE Trans. Geosci. Remote Sens.*, vol. 57, no. 4, pp. 2290–2304, Apr. 2018.

[32] M. Long, Y. Cao, Z. Cao, J. Wang, and M. I. Jordan, "Transferable representation learning with deep adaptation networks," *IEEE Trans. Pattern Anal. Mach. Intell.*, vol. 41, no. 12, pp. 3071–3085, Dec. 2019.

[33] B. Guo, T. Liu, X. Zhang, and Y. Gu, "Few-shot multispectral-hyperspectral image collaborative classification with feature distribution enhancement and subdomain alignment," *IEEE Trans. Geosci. Remote Sens.*, vol. 62, Jan. 2024, Art. no. 5505117, doi: 10.1109/TGRS.2024.3351846.

[34] Y. Zhang, W. Li, M. Zhang, Y. Qu, R. Tao, and H. Qi, "Topological structure and semantic information transfer network for cross-scene hyperspectral image classification," *IEEE Trans. Neural Netw. Learn. Syst.*, vol. 34, no. 6, pp. 2817–2830, Jun. 2023, doi: 10.1109/TNNLS.2021.3109872.

[35] Y. Qu, R. K. Baghbaderani, W. Li, L. Gao, Y. Zhang, and H. Qi, "Physically constrained transfer learning through shared abundance space for hyperspectral image classification," *IEEE Trans. Geosci. Remote Sens.*, vol. 59, no. 12, pp. 10455–10472, Dec. 2021, doi: 10.1109/TGRS.2020.3045790.

[36] A. Bendale and T. E. Boult, "Towards open set deep networks," in *Proc. IEEE Conf. Comput. Vis. Pattern Recognit.*, 2016, pp. 1563–1572.

[37] R. P. W. Duin and E. Pekalska, "Open issues in pattern recognition," in *Computer Recognition Systems*. Berlin, Germany: Springer, 2005, pp. 27–42.

[38] K. Saito, S. Yamamoto, Y. Ushiku, and T. Harada, "Open set domain adaptation by backpropagation," in *Proc. Eur. Conf. Comput. Vis.*, 2018, pp. 153–168.

[39] Z. Fang, J. Lu, F. Liu, J. Xuan, and G. Zhang, "Open set domain adaptation: Theoretical bound and algorithm," *IEEE Trans. Neural Netw. Learn. Syst.*, vol. 32, no. 10, pp. 4309–4322, Oct. 2021, doi: 10.1109/TNNLS.2020.3017213.

[40] H. Liu, Z. Cao, M. Long, J. Wang, and Q. Yang, "Separate to adapt: Open set domain adaptation via progressive separation," in *Proc. IEEE/CVF Conf. Comput. Vis. Pattern Recognit.*, 2019, pp. 2927–2936.

[41] P. R. M. Júnior et al., "Nearest neighbors distance ratio open-set classifier," *Mach. Learn.*, vol. 106, no. 3, pp. 359–386, Mar. 2017.

[42] J. Zhang, J. Liu, B. Pan, Z. Chen, X. Xu, and Z. Shi, "An open set domain adaptation algorithm via exploring transferability and discriminability for remote sensing image scene classification," *IEEE Trans. Geosci. Remote Sens.*, vol. 60, Sep. 2022, Art. no. 5609512, doi: 10.1109/TGRS.2021.3110060.